pp 21–41.
doi: 10.1017/aer.2017.109

Influence analysis of propeller location parameters on wings using a panel/viscous vortex particle hybrid method

H.B. Wang
whbxxf@mail.nwpu.edu.cn
Z. Zhou and X.P. Xu
College of Aeronautics
Northwestern Polytechnical University
Xi'an, China
Science and Technology on UAV Laboratory
Northwestern Polytechnical University
Xi'an, China

X.P. Zhu
Science and Technology on UAV Laboratory
Northwestern Polytechnical University
Xi'an, China

ABSTRACT

For aircraft that employ distributed propeller propulsion systems, the distributed propeller slipstream increases the analysis complexity. The objective of this paper is to rapidly analyse the influence of propeller slipstream on a wing using a fast prediction approach to perform conceptual design studies. This fast approach is implemented through a panel/viscous vortex particle hybrid method taking into account the air viscosity effect. The parametric studies of propeller streamwise, spanwise, vertical installed position, propeller number and rotational direction are conducted for a rectangular wing platform in two different propeller-wing configurations. The results indicate that the propeller slipstream causes both the augmentations of the wing lift and drag in a traditional tractor propeller layout. For an over-the-wing propeller configuration, however, the obvious lift increase and drag decrease can be obtained. A rear propeller position relative to the wing chord leads to a beneficial increase in lift while a fore propeller location is able to decrease the wing drag. The maximum increment of the lift-to-drag ratio can be achieved by 17.6% when the propeller is located at 30% of the wing chord, which shows a considerable advantage in improving the wing aerodynamic efficiency.

Keywords: Distributed propeller slipstream; panel/viscous vortex particle hybrid method; tractor propeller arrangement; over-the-wing propeller configuration

Received 19 January 2017; revised 18 September 2017; accepted 21 September 2017; first published online 26 October 2017.

NOMENCLATURE

ϕ	velocity potential function
∇^2	laplace operator
$\boldsymbol{n}$	normal vector of the body's surface
dS	elemental surface area
μ	doublet strength
σ	source strength
B	influence coefficient of a unit source strength
C	influence coefficient of a unit doublet strength
C_L	lift coefficient
C_D	drag coefficient
C_M	moment coefficient
C_T	propeller thrust coefficient $T/\rho\pi\Omega^2 R^4$
L/D	lift to drag ratio of the wing
C_p	pressure coefficient
N	number of vortex particle
$N_{\boldsymbol{B}}$	number of body surface panel
N_w	number of wake surface panel
S_B	body surface
S_w	wake surface
R	propeller or rotor radius
R_n	dimensionless distance
$\boldsymbol{V}_0$	free-stream velocity
$\boldsymbol{u}$	local fluid velocity
$\boldsymbol{u}_{\text{ind}}$	induced velocity of a vortex particle
v_{ref}	kinematic velocity
ΔS_k	body panel area
ΔF_k	aerodynamic force on the kth panel
ρ	density of air
Ω	the rotational speed of the body's frame of reference
ς_ε	gaussian distribution function
Δt	time step
ω	vector vorticity
ν	kinematic viscosity coefficient
$\boldsymbol{a}$	vorticity of particle
ε	smoothing parameter
V_q	induced velocity of particle
γ	surface vorticity

1.0 INTRODUCTION

The research on distributed electric propulsion (DEP) aircraft, such as solar-powered aircraft, has been motivated in recent years because of the beneficial increase in reliability, safety and total efficiency, and significant reductions in noise as well as system-level emissions. However, the distributed propellers' rotation will make a large part of an aircraft's wing immerged in the propeller slipstream, such as the Helios prototype solar-powered aircraft[1], whose propeller

https://doi.org/10.1017/aer.2017.109 Published online by Cambridge University Press

slipstreams cover more than 50% of the wing area. Distributed propeller slipstreams will cause mutual aerodynamic interactions between propellers and the wing, which can significantly affect the DEP aircraft's performance, stability and so on. Therefore, accurate and fast analysis is required to perform conceptual design for the DEP configuration and critical for avoiding the expensive modification at a later stage.

In recent years, the Computational Fluid Dynamics (CFD) technology has been successfully applied to numerically simulate the complicated flow for the propeller-driven aircraft or the rotorcraft. There are mainly three kinds of methods that have been developed, including the actuator disc method[2-4], the Multiple Reference Frame method[5] and the unsteady sliding mesh method[6,7]. Although the CFD method has a high fidelity in predicting the propeller-wing interference behaviour, its computational cost limits its own applications at conceptual and preliminary design stages of an aircraft. In addition, using only an experimental method to address the effect of the interaction is also not a viable option because of its high cost. In order to overcome the above issues, methods and tools capable of rapidly and accurately predicting propeller slipstream effects are required.

Panel methods[8-10] have been widely used to predict aerodynamic forces of aircraft during initial design studies because of their computational efficiency. Although easy to use, most modern panel methods still have severe drawbacks. The main drawbacks are the inviscid assumption and the singularity problem which occurs when wake panels are close to each other[11]. In addition, most panel-method implementations require the user's expertise and effort to specify wake positions. The unreasonable wake panel positions will result in unavoidable wrong calculation results. Therefore, the traditional panel method should be improved by combining another wake dynamic method to simulate complex wakes.

The free-wake method[12] is often coupled with the panel method to simulate the complex wakes of the rotor or the propeller by replacing the wake panels with vortex lattices; however, its result depends on empirical formulations such as the vortex decay factor or vortex core size and therefore its applications are also limited.

Compared with the free-wake method, the vortex particle method is a powerful numerical tool to solve the flow around the complex geometries. The wake of the lifting surface is modelled with vortex particles[13] and there are fewer empirical parameters. This approach has been combined with a panel method to predict the aircraft's aerodynamic forces[13-16]. However, the flow viscosity effect is neglected in these studies.

In this paper, a panel/viscous vortex particle hybrid method, considering the flow viscosity, is developed. The aerodynamic force on the body's surface is determined by the panel method while the wake surface shed by the trailing edge of the wing is described using the viscous vortex particle method. In order to establish the relationship between the panel and the vortex particle method, the procedure of converting a wake panel doublet to a vortex particle vorticity is necessary and important. In addition, the influence of the wake vortex particle on a body panel is also implemented according to the Neumann boundary condition.

The present study analyses the wing aerodynamic behaviour under the influence of the propeller slipstream. As a first step, the panel/viscous vortex particle hybrid method is presented and the method validation is conducted by comparing with experimental results. As a further step, the propeller installed position, the propeller number and its rotational direction are discussed for two kinds of propeller-wing configurations, i.e. a tractor propeller configuration and an over-the-wing propeller configuration, to investigate the aerodynamic behaviour of the wing influenced by the propeller.

https://doi.org/10.1017/aer.2017.109 Published online by Cambridge University Press

2. COMPUTATION METHOD

In this section, the panel method (Section 2.1), the viscous vortex particle method (Section 2.2) are described respectively. In order to establish the relationship between these two approaches, a Hess's demonstration is used to convert a doublet wake into a vortex wake (Section 2.3). In addition, the influence of the wake vortex particle on the body panel is considered and implemented by using the Neumann boundary condition (Section 2.4). Lastly, two wind tunnel models with experimental data are used to perform the method validation in Section 2.5.

2.1 Panel method

Consider a body with known boundaries moving in a potential flow which is irrotational, inviscid and incompressible, the continuity equation can be simplified to Laplace's equation[17]:

$$\nabla^2\phi = 0 \qquad \ldots(1)$$

where ∇^2 is the Laplace operator, ϕ is a velocity potential function. According to Green's identity, the solution to Equation (1) can be constructed by a sum of source σ and doublet μ distributions on the known body boundary S_B and the wake boundary S_w:

$$\frac{1}{4\pi}\int_{S_B}\mu\boldsymbol{n}\cdot\nabla\left(\frac{1}{r}\right)dS - \frac{1}{4\pi}\int_{S_B}\sigma\left(\frac{1}{r}\right)dS + \frac{1}{4\pi}\int_{S_w}\mu\boldsymbol{n}\cdot\nabla\left(\frac{1}{r}\right)dS = 0 \qquad \ldots(2)$$

where $\boldsymbol{n}$ is the normal vector of the body's surface and r is a distance between an arbitrary point in the flow field and its coordinate system's origin, and dS is the elemental surface area.

2.1.1 Boundary condition

For a solid surface, there should be no flow flux penetrating it along its normal vector direction, which means a zero normal velocity on the boundaries should be specified. This direct formulation is called the Neumann boundary condition. According to this boundary condition, the source strength σ can be solved by

$$\sigma = -\boldsymbol{n}\cdot\boldsymbol{V}_0 \qquad \ldots(3)$$

where $\boldsymbol{V}_0$ is the free-stream velocity.

In this paper, a constant strength rectilinear panel is assumed. After dividing the body and wake surfaces into N_B quadrilateral body panels and N_w quadrilateral wake panels, Equation (2) can be transformed into the following form:

$$\sum_{k=1}^{N_B} C_k\mu_k + \sum_{w=1}^{N_w} C_w\mu_w + \sum_{k=1}^{N_B} B_k\sigma_k = 0 \qquad \ldots(4)$$

where C_k, B_k are the influence coefficients of the panel k on an arbitrary point induced by a unit doublet strength and a unit source strength, respectively.

By using the Kutta condition, the unknown wake doublets μ_w can be replaced by two corresponding unknown trailing-edge doublets μ_u, μ_l ("u" indicates the upper surface, while

https://doi.org/10.1017/aer.2017.109 Published online by Cambridge University Press

"*l*" the lower surface) of the wing:

$$\mu_w = \mu_u - \mu_l \quad \ldots (5)$$

Substitute Equation (5) into Equation (4), Equation (4) can be rewritten as

$$\sum_{k=1}^{N} A_k \mu_k = -\sum_{k=1}^{N} B_k \sigma_k \quad \ldots (6)$$

where $A_k = C_k$ if the panel is not at the trailing edge of the wing; if it is, then $A_k = C_k \pm C_w$.

2.1.2 Aerodynamic loads

When Equation (6) is solved, the source and doublet strengths of each panel can be obtained. Now, the pressure coefficient for each body panel can be computed as:

$$C_p = \frac{p - p_{ref}}{(1/2)\rho v_{ref}^2} = 1 - \frac{u^2}{v_{ref}^2} - \frac{2}{v_{ref}^2}\frac{\partial \phi}{\partial t} \quad \ldots (7)$$

where p and p_{ref} are the local pressure and far field reference pressure, u is the local fluid velocity, v_{ref} is the reference velocity and ρ is the density of the air.

In terms of the pressure coefficient the aerodynamic force ΔF_k contributed by the kth body panel with an area of ΔS_k is

$$\Delta F_k = -C_{pk}\left(\frac{1}{2}\rho v_{ref}^2\right)_k \Delta S_k \boldsymbol{n}_k \quad \ldots (8)$$

2.2 Viscous vortex particle method

2.2.1 Vorticity dynamics equation

In order to avoid the singularity problem mainly caused by wake panels, the vortex particle method[16,18,19] is used to model the vorticity in the wake domain. For an incompressible flow, the Navier-Stokes equation can be expressed in the velocity-vorticity form as follows:

$$\frac{\partial \boldsymbol{\omega}}{\partial t} + \boldsymbol{u} \cdot \nabla \boldsymbol{\omega} = \nabla \boldsymbol{u} \cdot \boldsymbol{\omega} + \nu \nabla^2 \boldsymbol{\omega} \quad \ldots (9)$$

where ω is vector vorticity, ν is kinematic viscosity coefficient and $\boldsymbol{u}$ is the local fluid velocity.

To solve Equation (9), the continuity vorticity field can be represented by the sum over all of the discrete vortex particles as:

$$\boldsymbol{\omega}_\varepsilon^h(x, t) = \sum_{q=1}^{N} \boldsymbol{a}_q(t) \varsigma_\varepsilon[\boldsymbol{x} - \boldsymbol{x}_q(t)] \quad \ldots (10)$$

https://doi.org/10.1017/aer.2017.109 Published online by Cambridge University Press

where N represents the number of vortex particle, $\boldsymbol{a}_q(t)$ and $\boldsymbol{x}_q$ are the vector-valued vorticity and the position of the particle q, respectively, ς_ε is the Gaussian distribution function

$$\varsigma_\varepsilon(R_n) = \frac{1}{(2\pi)^{3/2}\varepsilon^3} e^{-R_n^2/2} \quad \ldots(11)$$

where $R_n = |\boldsymbol{x} - \boldsymbol{x}_q|/\varepsilon$ is the dimensionless distance between an arbitrary point in the fluid field and the particle q and ε is the smoothing parameter.

When the continuity vorticity field is discretised by N vortex particles, the governing Equation (9) can be divided into two equations as follows:

$$\frac{\partial \boldsymbol{x}}{\partial t} = \boldsymbol{V}_0 + \boldsymbol{u}_{\text{ind}} \quad \ldots(12)$$

$$\frac{d\boldsymbol{a}_p}{dt} = \boldsymbol{a}_p \cdot \nabla \boldsymbol{u}(x_p, t) + \nu \nabla^2 \boldsymbol{a}_p \quad \ldots(13)$$

2.2.2 Vortex stretching effect

In Equation (13), the first term in the right-hand side is called the stretching effect, which describes the vortex stretching and rotation due to the velocity gradient. In this paper, the so-called direct scheme method[19,20] is used to solve this term:

$$\left.\frac{d\boldsymbol{a}_p}{dt}\right|_{ST} = \boldsymbol{a}_p \cdot \nabla \boldsymbol{u}\left(x_p, t\right) = \left[\nabla \boldsymbol{u}\left(\boldsymbol{x}_p, t\right)\right]\left[\boldsymbol{a}_p\right] \quad \ldots(14)$$

where $\nabla \boldsymbol{u}(x_p, t)$ is the velocity gradient and its expression form is described in Ref. 19.

2.2.3 Viscous diffusion effect

The second term in the right-hand side of Equation (13) represents the viscous diffusion effect, which describes the air viscosity through the vorticity transportation. This term, neglected in Refs (13–16), is considered in this paper and its solution can be derived using the particle strength exchange (PSE) method[21]. The basis of this approach is using an integral operator to approximate the Laplacian operator, and the expression form can be written as

$$\left.\frac{d\boldsymbol{a}_p}{dt}\right|_{VDT} = \nu \nabla^2 \boldsymbol{a}_p = \frac{2\nu}{\hat{\varepsilon}^2} \sum \varsigma_\varepsilon \left(V_p \boldsymbol{a}_q - V_q \boldsymbol{a}_p\right)\left(\boldsymbol{x}_p - \boldsymbol{x}_q\right) \quad \ldots(15)$$

where V_p and V_q are the volumes of particles p and q.

2.3 Conversion of doublet wakes to vortex wakes

The vortex-particle method is used to determine the wake domain vorticity after the potential flow on the body has been solved using the panel method. In order to establish the relationship between these two approaches, a procedure of converting double wakes to vortex-particle wakes is indispensable.

The wake model shed by the body trailing edge is composed of two parts: a doublet buffer wake sheet and a vortex-particle vortex[18] (see Fig. 1). The doublet buffer wake sheet is shed from the trailing edge of a lifting surface, and it has the same amount of panels as the trailing edge along the wing spanwise direction. In the streamwise direction, there are two rows of

https://doi.org/10.1017/aer.2017.109 Published online by Cambridge University Press

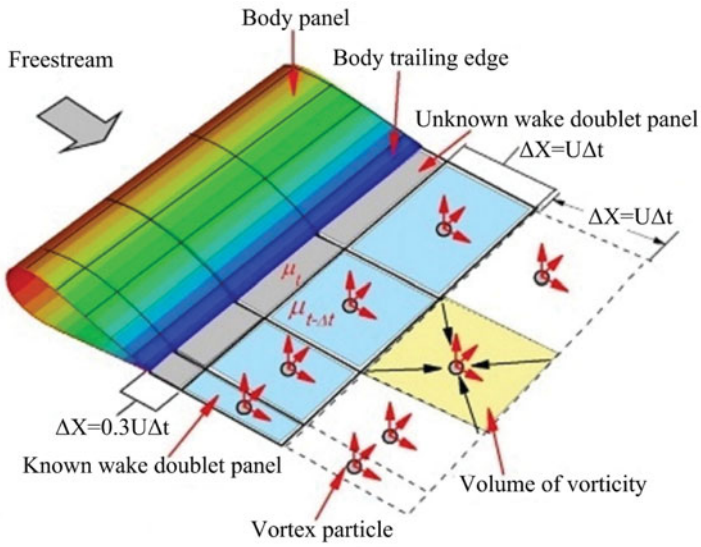

Figure 1. (Colour online) Conversion of constant strength wake doublet panels to vortex particles.

panels in the buffer wake sheet. The first row, which has a length of $0.3U\Delta t$ [16], is adjacent to the lifting-surface trailing edge and its doublet strength is determined by the Kutta condition. It is assumed that wake panels in the first row have constant doublet strength when they travel to the downstream positions. The second row has a length of $U\Delta t$ and its doublet strength is equal to that at the previous time-step. In this row, the known doublet wake panels are converted into the equivalent vortex particles.

The relationship between doublet wake panels and vortex particles can be established by Hess's demonstration[22] as depicted in Equation (16), which indicates that the velocity at an arbitrary point in the flow domain caused by a doublet surface is equal to the sum of the velocities induced by both a vortex sheet of strength $\gamma = \mathbf{n} \times \nabla\mu$ on S_w and a vortex filament of strength μ around the perimeter of the given panel C_w.

$$u_\mu(x) = \frac{1}{4\pi}\int_{C_W} \mu \frac{d\boldsymbol{l} \times \boldsymbol{r}}{r^3} ds - \frac{1}{4\pi}\int_{S_w} \boldsymbol{\gamma} \times \frac{\boldsymbol{r}}{r^3} ds \qquad \ldots (16)$$

2.4 Particle influence on panels

It is obvious that the vortex-particle wake has important influence on the body panel. When the vortex particles are included, their influences can be accounted for by adding the induced velocities of all wake particles into the Neumann boundary condition. Therefore, the new source strength[23] of each panel can be rewritten as

$$\sigma = -\boldsymbol{n} \cdot \left(\boldsymbol{V}_0 + \sum_{q=1}^{N} \boldsymbol{u}_{\text{ind}}^q \right) \qquad \ldots (17)$$

where $\boldsymbol{u}_{\text{ind}}^q$ is the induced velocity of the particle q, it can be obtained through the Biot-Savart law.

https://doi.org/10.1017/aer.2017.109 Published online by Cambridge University Press

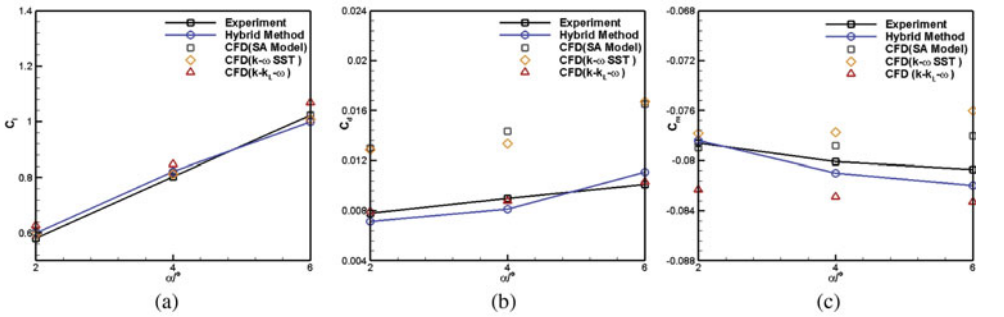

Figure 2. (Colour online) Aerodynamic forces comparison of E387 aerofoil. (a) Lift coefficient. (b) Drag coefficient. (c) Moment coefficient.

2.5 Validation

In order to validate the proposed panel/viscous vortex particle hybrid method, two wind tunnel models with experimental data are used to make comparisons with our calculation results. The first model, i.e. a low Reynolds number aerofoil Eppler 387, is used to validate the accuracy of the wing drag because the viscosity effect of the air is considered in the hybrid method. The second one is a two-blade rotor, which is utilised for the purpose of demonstrating the accuracy of the hybrid method for the rotating machinery. For the panel method, panel density has an important effect on the calculated results, and the sensitivity of this method to panel density has been investigated by many researchers[24-27]. In this section, the Eppler 387 aerofoil is modelled by 40 chordwise panels and the rotor is panelled with 30 chordwise panel rows and 20 spanwise panel columns.

2.5.1 *Example 1: E387 aerofoil*

Computational results for the E387 aerofoil are described in Fig. 2 and compared with experimental data[28] and CFD results. The Reynolds number based on the aerofoil chord is $\mathrm{Re} = 4.6 \times 10^5$ and the Mach number is 0.13. CFD simulations are conducted using the commercial software ANSYS Fluent. The RANS solver is used for all computations. The first grid node near the wall is placed at $y^+ < 1$. Considering the important effect of the turbulence model on the numerical simulation result, the Spalart-Allmaras[29] (SA) and Menter's k-ω SST[30] turbulence models as well as the k-k_L-ω transition model[31] are selected to analyse the turbulence model sensitivity.

The results presented in Fig. 2 indicate that the lift coefficients obtained with both the turbulence model and the transition model show good agreements with experimental data. However, the k-k_L-ω transition model is more accurate than the turbulence models in predicting the drag and pitching moment of the wing for a low Reynolds number flow. The difference between the turbulence model and the transition model is that the transition model has the ability of correctly describing the transition from a laminar flow to a turbulent flow which often occurs in the practical situation. Owing to the difference above, the lift of the aerofoil solved by the turbulence model is a little smaller than that for the transition model but the drag, especially the skin-friction drag, is overestimated. Because of these discrepancies in lift and drag of the aerofoil, the pitching moment calculated by the turbulence model is less accurate than that for the transition mode, especially when the free-stream angle is increased.

https://doi.org/10.1017/aer.2017.109 Published online by Cambridge University Press

Table 1
Force measurements comparison

Method	C_T	Error
Exp	0.00459	-
CFD	0.00466	1.5%
Hybrid	0.00473	3.1%

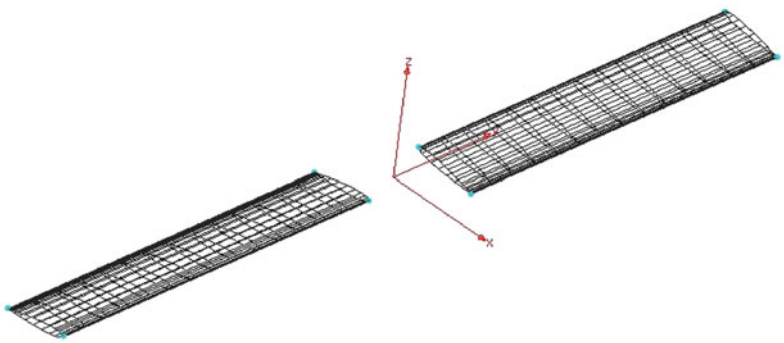

Figure 3. (Colour online) Panel model of a two-blade rotor.

For all these reasons, the k-k_L-ω transition model will be used for all the subsequent CFD calculations in this paper.

2.5.2 Example 2: helicopter rotor

In this example, we demonstrate the accuracy of the hybrid method by rotating a pair of high aspect ratio and untwisted wings (see Fig. 3) in hovering condition. This two-blade rotor[32] uses a NACA0012 profile and has a collective pitch angle of $a = 8°$. The aspect ratio of a single blade is 6 and the rotational speed in this experiment is 1250 r/min.

In Table 1, the rotor thrust coefficient obtained from the current method is also compared with the experimental data and CFD results. There is only a small difference between them, showing a good accuracy of this hybrid method.

The chordwise pressure distribution for two blade sections is given in Fig. 4. It can be seen that the calculation results of the panel/vortex-particle hybrid method are close to the CFD results and the experimental data[32], which were measured in the U.S. Army Aeromechanics Laboratory. The accuracy of the hybrid method is desirable for the purpose of fast prediction of the overall aerodynamic force.

3. RESULTS AND DISCUSSIONS

3.1 The tractor propeller configuration

In this section, the wing's aerodynamic behaviours affected by the propeller for a tractor propeller configuration (Fig. 5) are investigated using the panel/vortex-particle hybrid method. The rectangular wing has an aspect ratio of 2 and is modelled by 40 chordwise and 20 spanwise panels totaling 800 panels. The Reynolds number based on the root chord of

https://doi.org/10.1017/aer.2017.109 Published online by Cambridge University Press

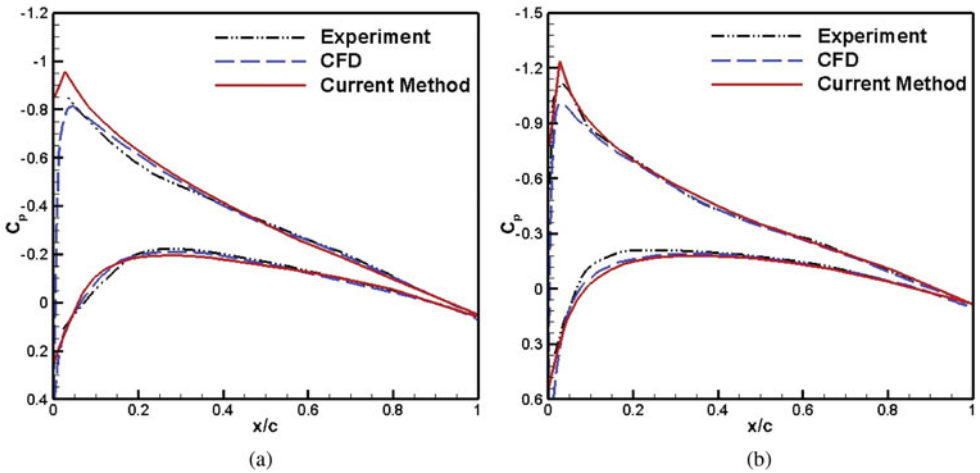

Figure 4. (Colour online) Chordwise pressure distribution at different radial sections on one rotor blade. (a) r/R = 0.5. (b) r/R = 0.8.

Figure 5. (Colour online) Single tractor propeller-wing configuration.

the wing is $Re = 4.88 \times 10^5$ at the flight altitude of 20 km. The free-stream velocity direction points in the positive x axis and the angle-of-attack is selected as 2°. The propeller we designed has a rotational speed of 1500 r/min and a clockwise rotational direction observed from the downstream position. It is panelled with 30 chordwise panel rows and 20 spanwise panel columns.

A comparison of aerodynamic coefficients between the CFD method and the hybrid method is presented in Table 2. For the CFD method, two different mesh densities, i.e. a coarse grid of 5.2 million cells and a fine grid of 9.5 million cells, have been tested to see their influence on the calculation results. As can be seen, there is small difference in the wing's lift, pitching moment and the propeller thrust between these two methods. Considering the results solved by two different mesh densities for the CFD method are very close to each other, all the subsequent calculations for the CFD method are conducted with the 5.2 million cells grid.

Compared with the drag coefficient provided by the CFD method, there is a relatively larger drag error for the hybrid method even if the drag error can be reduced to be 6.25% with a fine mesh grid. In future work, it is necessary for us to study some relevant calculation parameters'

https://doi.org/10.1017/aer.2017.109 Published online by Cambridge University Press

Table 2
Comparison of aerodynamic coefficients

Method	C_L	C_D	C_M	C_T
CFD(coarse grid)	0.2932	0.0212	–0.0729	0.0561
CFD(fine grid)	0.2914	0.0208	–0.0723	0.0559
Hybrid Method	0.2980	0.0195	–0.0741	0.0548
Error(coarse grid)	1.64%	–7.97%	1.65%	–2.31%
Error(fine grid)	2.26%	–6.25%	2.49%	–1.86%

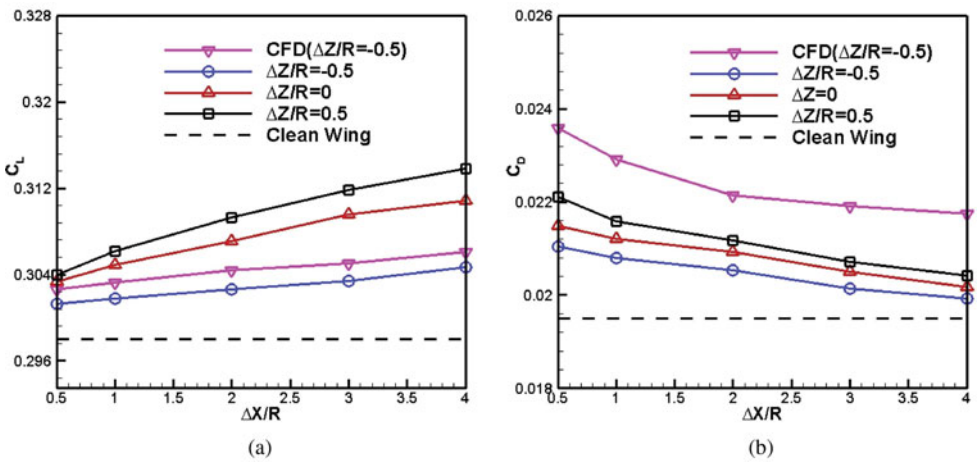

Figure 6. (Colour online) Effect of propeller chordwise position on lift and drag coefficients of the wing. (a) Lift coefficient. (b) Drag coefficient.

effect (such as the panelling density) in detail and update the unreasonable parameter used in the hybrid method for the purpose of further reducing the calculation error, especially the drag error, between the hybrid method and the experiment or the CFD method.

3.1.1 Effects of the streamwise position

Figure 6 presents the effects of propeller chordwise and vertical installed positions on the wing's aerodynamic performance. In this figure, R is the propeller radius, $\Delta X/R$ and $\Delta Z/R$ are the dimensionless horizontal and vertical distances between the propeller rotation centre and the leading edge of the wing, respectively. A positive value of $\Delta Z/R$ means the propeller is installed at a high vertical position relative to the wing.

It is clearly shown that the propeller slipstream leads to the increases of the lift and the drag on the wing. For example, when the propeller is installed at the position ($\Delta X/R = 0.5$, $\Delta Z/R = 0.5$), there is only a 2.01% increment in the lift coefficient but a 13.3% augmentation in the drag coefficient, as a result, the lift-to-drag ratio is decreased by 10%. In addition, it is apparent that a far horizontal position and a high vertical installed position of the propeller relative to the wing's leading edge are favourable for increasing the wing's lift and decreasing the drag.

https://doi.org/10.1017/aer.2017.109 Published online by Cambridge University Press

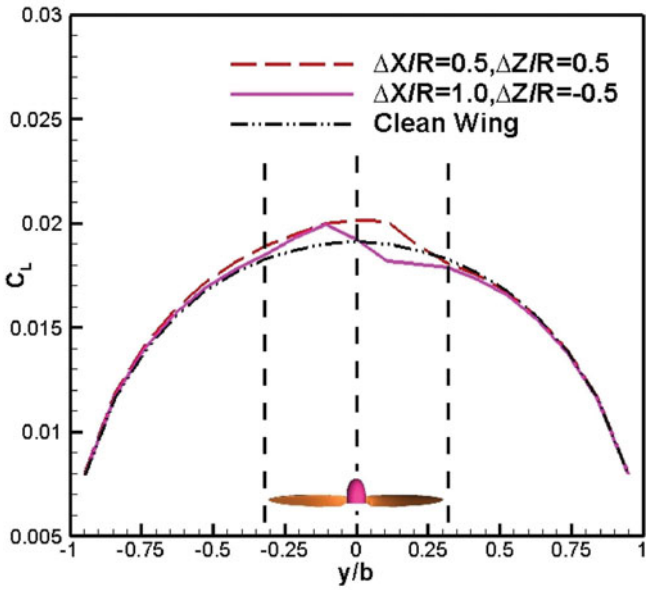

Figure 7. (Colour online) Spanwise lift distribution of the wing with the influence of a single propeller.

The main reason of the augmentations of the wing's lift and drag can be attributed to the increased total and dynamic pressures of the propeller slipstream because of the propeller rotation. The increased dynamic pressure causes an acceleration of the axial velocity after the propeller, as a result, the propeller slipstream contracts its stream tube according to the principle of mass conservation. When the slipstream encounters the wing located at the downstream position, the contraction of the stream tube is strengthened and a more lift augmentation is obtained.

Besides the acceleration of the axial velocity, a tangential velocity component is also produced by the propeller rotation. The tangential velocities distributed at two sides of the propeller axis have equal magnitudes but opposite directions. For a traditional tractor propeller configuration, this tangential velocity distribution induces both upwash and downwash regions on the wing surface. In the upwash region, the effective local angle-of-attack is increased, which generates an augmentation of the section lift of the wing. In the downwash region, however, the down-going propeller blade leads to the decrease of the effective local angle-of-attack, so the section lift of the corresponding wing area is reduced.

Because of the upwash and downwash regions generated by the propeller, the distribution of the spanwise load of the wing has phenomena of peak and trough at two sides of the propeller axis as illustrated in Fig. 7. It can be clearly seen that the range of the wing affected by the propeller slipstream is almost equal to the propeller diameter. The rotational direction and installed position of the propeller will determine the locations of the load peak as well as trough and dominate the final shape of the spanwise load distribution of the wing.

For a subsonic flow, there is a mutual interaction between the propeller and the wing. The propeller slipstream, significantly affecting the wing's aerodynamic behaviour, also conversely affects its own performance. Figure 8 shows the changes of propeller thrust coefficient versus five chordwise positions and three vertical positions of the propeller. CFD simulation results

https://doi.org/10.1017/aer.2017.109 Published online by Cambridge University Press

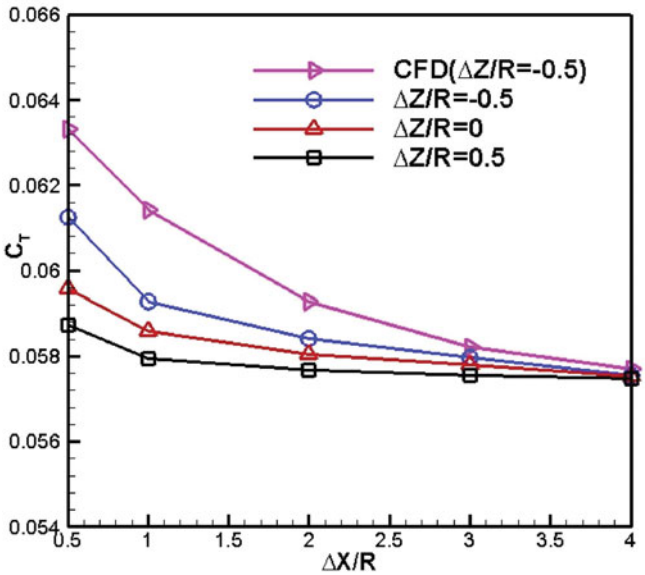

Figure 8. (Colour online) Effect of streamwise locations of the single propeller on propeller thrust coefficient.

are also given for the purpose of comparisons. The maximum difference between the current approach and the CFD method is only 3.5%, which shows a good accuracy of the hybrid method used in this paper.

It indicates that an increased chordwise distance leads to a decreasing propeller thrust coefficient and the propeller thrust falls slowly when $\Delta X/R > 2$. Because the wing is located downstream from the propeller, it decreases the velocity of the propeller slipstream but increases the slipstream's static pressure behind the propeller disk. This is so-called the wing's aerodynamic interference on the propeller and it is helpful to augment the propeller thrust. However, this beneficial interference will be quickly weakened as the chordwise distance is enlarged, as a result, the propeller thrust at a larger $\Delta X/R$ is smaller than that at a smaller $\Delta X/R$. In addition, Fig. 8 also indicates that a lower vertical propeller position is favourable for the propeller thrust.

3.1.2 *Effects of the spanwise position*

The influence of the propeller spanwise position on the wing is investigated in this section. In Fig. 9, the results are depicted corresponding to a propeller chordwise position $\Delta X/R = 1.0$ and a vertical position $\Delta Z/R = -0.5$.

Compared with the clean wing, the benefits, i.e., a lift increase and a drag decrease, can be obtained apparently when the propeller is moved from the left tip ($y/b = -1$) to the right tip ($y/b = 1$) of the wing. The main reason for this result is the coaction of the upwash and downwash effects of the propeller on the wing. As described above, the propeller rotates clockwise observed from a downstream position. When it is mounted at the left tip of the wing, only the propeller downwash directly washes the wing. This downwash effect leads to the decreased effective angle-of-attack, as a result, less lift but more induced drag are generated in this case. On the contrary, when the propeller is installed at the right wing tip, it is the

https://doi.org/10.1017/aer.2017.109 Published online by Cambridge University Press

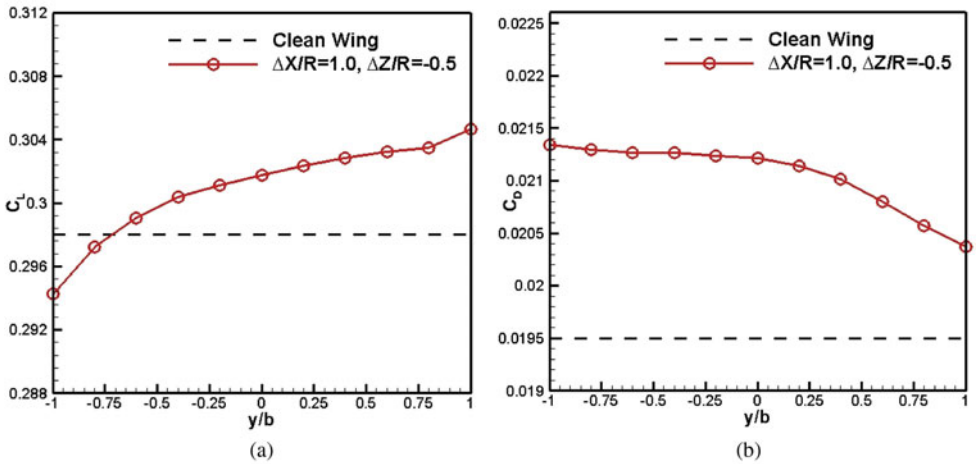

Figure 9. (Colour online) Effect of propeller spanwise positions on the wing. (a) Lift coefficient. (b) Drag coefficient.

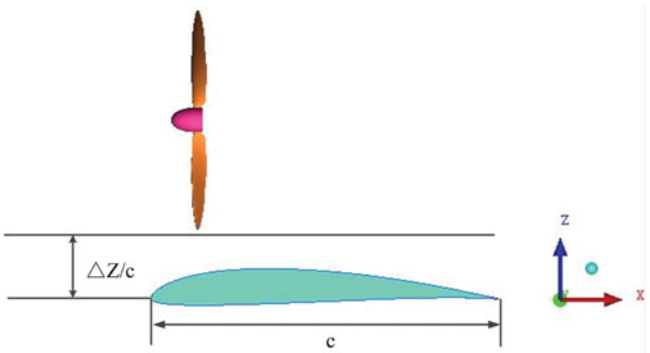

Figure 10. (Colour online) Over-the-wing propeller (OTWP) configuration.

propeller upwash that directly influences the wing. The increased effective angle-of-attack creates a bigger lift and a smaller induced drag.

3.2 The over-the-wing propeller configuration with a single propeller effect

The calculation results described in Fig. 6 indicates that the lift increment and the drag decrement can be obtained when the propeller is moved upward. This is because the high vertical installed propeller position makes the propeller slipstream mainly affect the upper surface of the wing and the velocity of the flow around the wing's upper surface is accelerated by the propeller rotation.

Inspired by this result, a new propeller-wing configuration (see Fig. 10), i.e. an over-the-wing propeller (OTWP) configuration is investigated in this section. In this configuration, the propeller is located over the wing in order to make the entire propeller slipstream beneficially influence the wing's upper surface.

https://doi.org/10.1017/aer.2017.109 Published online by Cambridge University Press

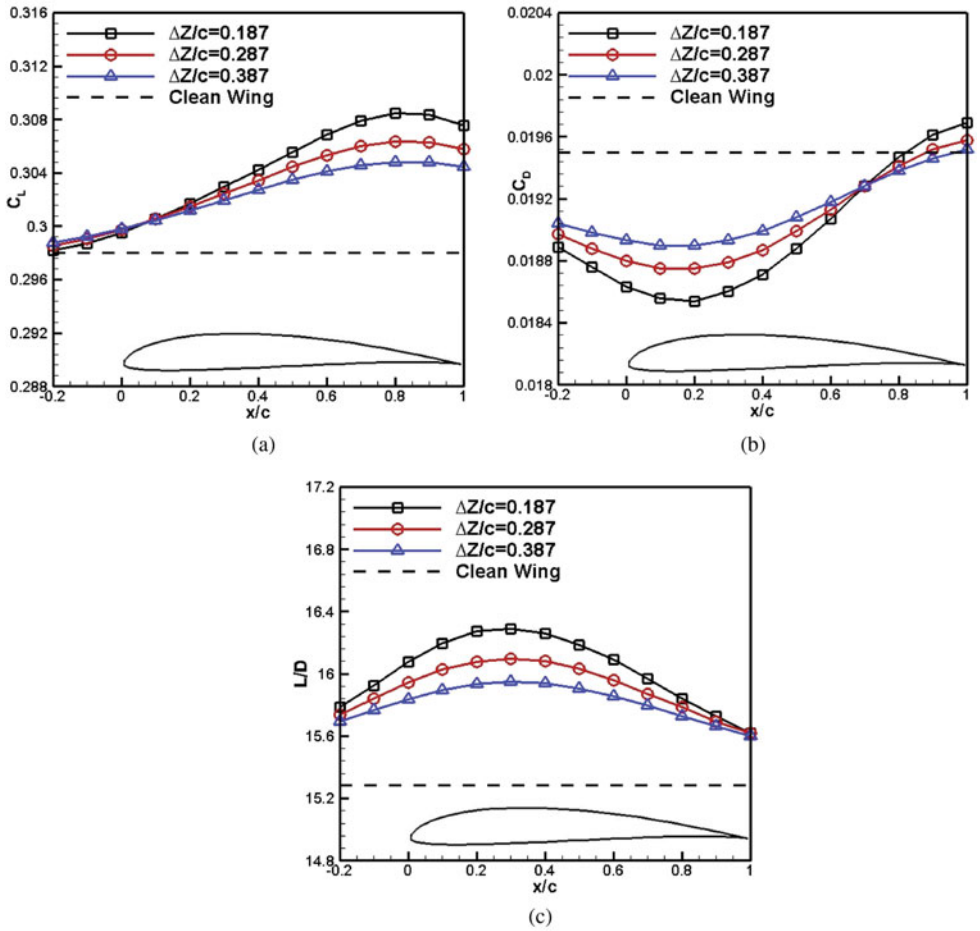

Figure 11. (Colour online) Effect of propeller chordwise positions on the OTWP configuration with a single propeller. (a) Lift coefficient. (b) Drag coefficient. (c) Lift-to-drag ratio.

In Fig. 11, the aerodynamic behaviour of the wing versus the propeller chordwise position is depicted for three clearance values of $\Delta Z/c = 0.187, 0.287, 0.387$.

Compared with the results presented in Fig. 6, the OTWP arrangement has favourable effects on both the lift and the drag of the wing, i.e. significant lift increment and drag reduction can be obtained. The maximum of the lift gain corresponds to the propeller chordwise position of $x/c = 0.8$, the maximal drag reduction occurs at $x/c = 0.2$, but the maximum lift-to-drag ratio is found at $x/c = 0.3$.

For the OTWP configuration, there is no propeller slipstream that directly washes the wing so that the acceleration of the axial free-stream velocity plays a more important role than the upwash and downwash effects of the propeller in changing the wing's aerodynamic performance. Because of the propeller's rotation, the dynamic pressure of the uniform free-stream in front of the propeller is increased, as a result, a region with a smaller static pressure on the upper surface of the wing is created, which is responsible for the lift augmentation when the propeller is moved backward.

https://doi.org/10.1017/aer.2017.109 Published online by Cambridge University Press

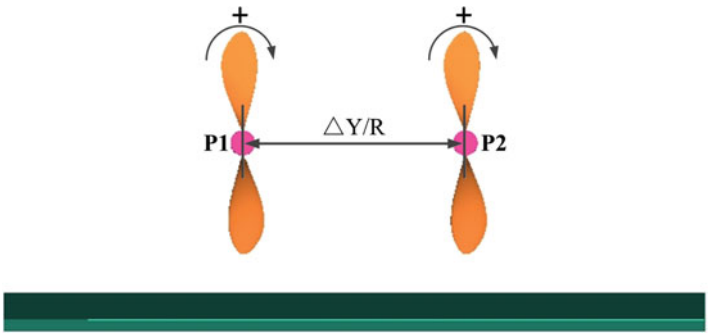

Figure 12. (Colour online) OTWP configuration with double propellers.

The reduction in the drag of the wing is the key aerodynamic feature of this configuration and it benefits from two parts: a suction effect and a pushing effect. For the flow in front of the propeller disc, the velocity is accelerated by the propeller so that the leading-edge suction force of the wing is enhanced and it creates a suction effect that slightly pulls the wing forward. For the flow behind the propeller disc, however, both the total and static pressures are increased and a pushing effect is generated. This effect generates a pushing force acting on the rear segment of the wing to further decrease the wing drag.

3.3 The OTWP configuration with double propellers effect

The results of the OTWP configuration described above have proved its considerable advantages to improve the aerodynamic performance of the wing. In order to exploit more benefits in this arrangement, double propellers are utilised to further investigate this configuration. The clearance between the propeller tip and the wing's leading edge is selected as $\Delta Z/c = 0.187$ and the rotational speed of these two propellers is still 1500 r/min.

As for double propellers, their rotational direction is an important factor affecting the performance of the wing. The OTWP configuration with double propellers is shown in Fig. 12 with a rear view. The plus sign represents the positive rotational direction of the propeller, i.e. the clockwise rotational direction. If both of these two propellers rotate with positive directions, we denote them as (P1+, P2+). In this section, two kinds of propeller rotational directions, i.e. (P1+, P2+) and (P1+, P2-), are selected for the simulations.

3.3.1 Streamwise position effect

The effect of the double propellers' streamwise position on the wing is presented in Fig. 13. As can be seen, the position where the maximum of the wing lift can be obtained is still at $x/c = 0.8$ (Fig. 13(a)) and the maximum of the lift-to-drag ratio also occurs at $x/c = 0.3$ (Fig. 13(c)). It should be mentioned that the spanwise distance between the double propellers is selected as $\Delta Y/R = 2.5$ and kept as a constant value ($\Delta Y/R$ is the dimensionless spanwise distance in Fig. 12) in order to make sure that there is only one propeller parameter that is investigated.

Although the trends of these curves are as the same as that shown in Fig. 11, the magnitudes of the lift and the lift-to-drag ratio are apparently raised and the drag is further reduced compared with the OTWP configuration with a single propeller. This phenomenon can be explained by the enhanced suction effect and pushing effect on the wing's upper surface caused by two propellers. The detailed calculation results corresponding to the propeller chordwise position $x/c = 0.3$ are depicted in Table 3. It is evident that the slipstream of

https://doi.org/10.1017/aer.2017.109 Published online by Cambridge University Press

Table 3
Comparison of OTWP configuration results with single-propeller and double-propellers

			Double Propellers	
	Clean Wing	**Single Propeller**	**P1+, P2+**	**P1+, P2-**
C_L	0.2980	0.3030	0.3068	0.3099
C_D	0.0195	0.0180	0.01778	0.01725
L/D	15.28	16.83	17.26	17.97

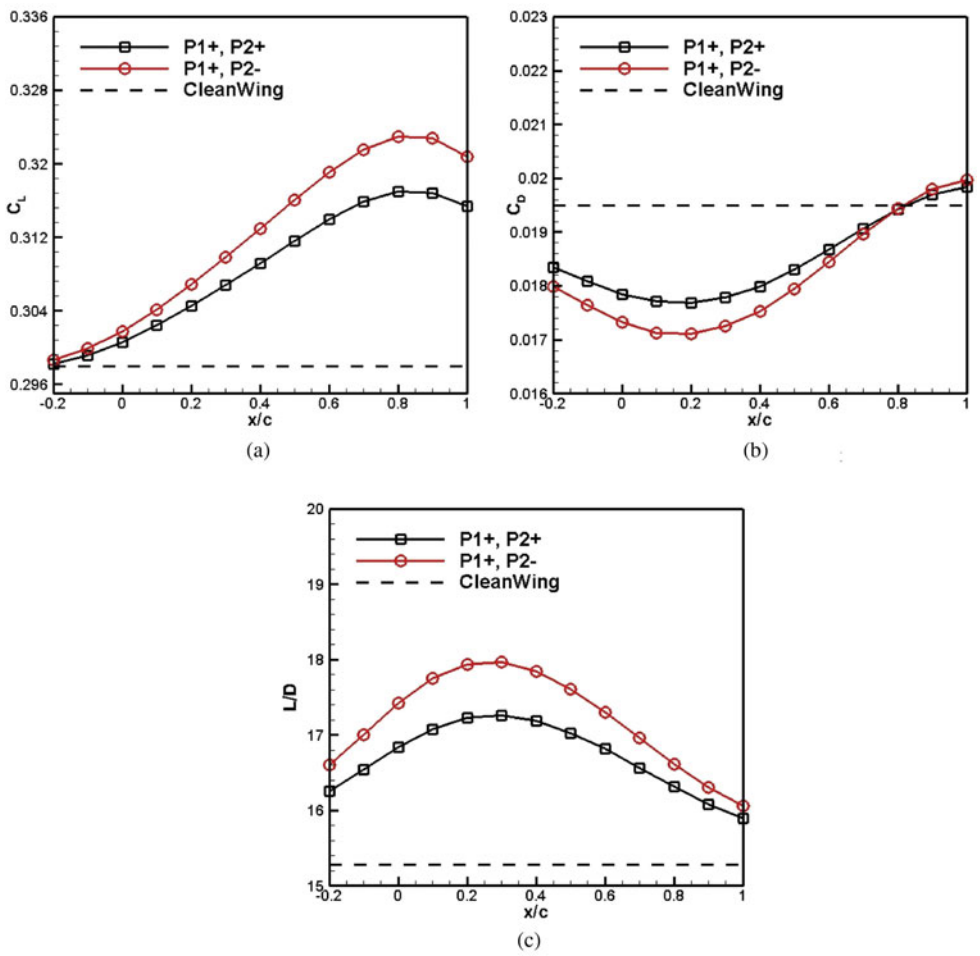

Figure 13. (Colour online) Effect of the double propellers' streamwise location on the OTWP configuration. (a) Lift coefficient. (b) Drag coefficient. (c) Lift-to-drag ratio.

https://doi.org/10.1017/aer.2017.109 Published online by Cambridge University Press

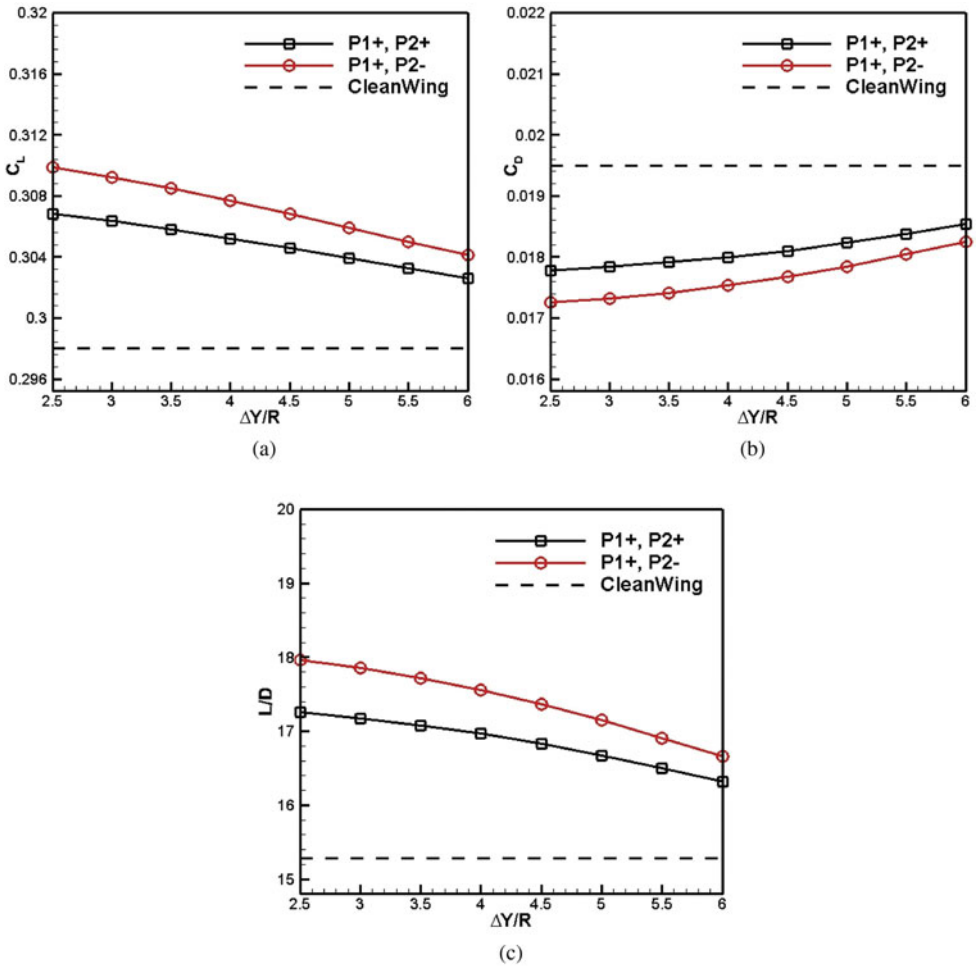

Figure 14. (Colour online) Effect of spanwise distance for the OTWP configuration with double propellers. (a) Lift coefficient. (b) Drag coefficient. (c) Lift-to-drag ratio.

the double propellers is more favourable than that of the single one for the performance of the wing. The increments of the lift, lift-to-drag ratio and the decrement of the drag can be achieved by 3.99%, 17.60% and 11.54%, respectively, relative to the clean wing.

3.3.2 *Spanwise position effect*

The spanwise distance between the two propellers is also important to affect the wing's aerodynamic behaviour. In this section, a range of $\Delta Y/R = 2.5$ to 6.0 is selected to perform the analysis. It should be explained that the value of $\Delta Y/R = 6$ corresponds to the location where these two propellers are mounted at two tips of the wing. Similarly, in order to ensure that there is only one influencing parameter, the double propellers' streamwise position is selected as $x/c = 0.3$. The results in Fig. 14 indicate that an increasing spanwise distance induces a decrement in the wing lift but an increment in the wing drag, and hence a decrease of

https://doi.org/10.1017/aer.2017.109 Published online by Cambridge University Press

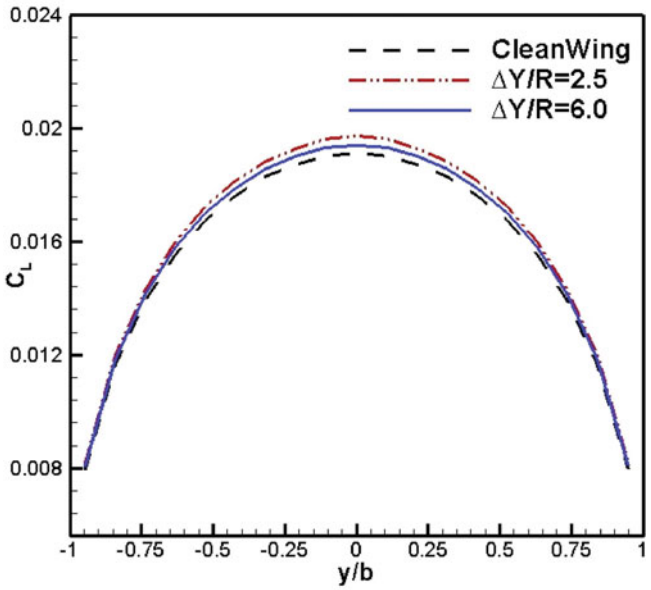

Figure 15. (Colour online) Spanwise lift distribution for the OTWP configuration with double propellers.

the lift-to-drag ratio. The reason for this unfavourable result is that a larger spanwise distance gradually abates the beneficial interactions between the double propellers and the wing.

In order to demonstrate the feature of the pressure distribution of the OTWP configuration, the spanwise load distributions at the positions $\Delta Y/R = 2.5$ and $\Delta Y/R = 6.0$ are plotted in Fig. 15. These curves indicate that the upwash and downwash regions occurring in a traditional tractor propeller arrangement vanish in the OTWP configuration. This is because there is no propeller slipstream directly washing the wing when the propeller is located over the wing and hence the effective angle-of-attack at the leading edge of the wing does not change significantly. Due to the disappearances of the upwash and downwash effects, the acceleration of the free-stream velocity becomes the major factor of improving the wing's aerodyanmic performance, which has been proved by the results in Fig. 15.

4. CONCLUSIONS

The present paper investigates the influence of the propeller location parameter on the wing aerodynamics using a panel/viscous vortex particle hybrid method. This method considering the air viscosity effects can accurately predict the wing's aerodynamic behaviour influenced by the propeller. Although it can't capture the detailed flow field characteristics, its computational cost is much lower than that of the CFD method and it can be used to rapidly obtain the wing overall aerodynamics to perform conceptual design studies.

For a traditional tractor-propeller configuration, the wing is immersed in the propeller slipstream and the accelerated free-stream velocity and the tangential velocity are induced by the propeller. Affected by these two effects, both the wing lift and drag are increased compared with that of the clean wing. When the propeller is located at a high vertical position, the wing aerodynamic performance can be improved slightly.

https://doi.org/10.1017/aer.2017.109 Published online by Cambridge University Press

The over-the-wing propeller (OTWP) configuration has advantages in increasing the wing lift and reducing the drag compared to the traditional propeller-wing layout. A small clearance between the propeller tip and the wing and a large propeller number are favourable to further improve the wing performance. For the double-propeller case, the maximum increment of the lift-to-drag ratio can be achieved by 17.6% when the propeller is located at 30% of the wing chord. Maybe the OTWP configuration is suitable for the distributed propulsion aircraft from the perspective of aerodynamics. Therefore, future work shall focus on the detailed investigation of the effects of the distributed propeller's parameters, including the propeller's number, the spanwise distance, and the rotational direction and speed, on the wing's aerodynamic performance in order to exploit more aerodynamic potentials of this new configuration.

REFERENCES

1. NOLL, T.E., ISHMAEL, S.D., HENWOOD, B., PEREZ-DAVIS, M.E., TIFFANY, G.C., MADURA, J., GAIER, M., BROWN, J. M. and WIERZBANOWSKI, T. Technical findings, lessons learned, and recommendations resulting from the helios prototype vehicle mishap, NASA 20070022260, 2007, Hampton, Virginia, US.
2. THOUAULT, N., BREITSAMTER, C., GOLOGAN, C. and ADAMS, N.A. Numerical analysis of design parameters for a generic fan-in-wing configuration, *Aerospace Science and Technology*, 2010, **14**, (1), pp 65-77.
3. FARRAR, B. and AGARWAL, R. CFD Analysis of open rotor engines using an actuator disk model, *52nd AIAA Aerospaces Science Meeting*, AIAA 2014-0408, 2014, National Harbor, Maryland, US.
4. VELDHUIS, L.M. and LUURSEMA, G.W. Comparison of an actuator disk and a blade modeling approach in Navier-Stokes calculations on the SR-3 propfan, *18th Applied Aerodynamics Conference*, AIAA 2000–4528, 2000, Denver, Colorado, US.
5. HU, D.M., OUYANG, H. and DU, Z.H. A study on stall-delay for horizontal axis wind turbine, *Renewable Energy*, 2006, **31**, (6), pp 821-836.
6. LIU, T.L. and PAN, K.C. Application of the sliding mesh technique for helicopter rotor flow simulation, *J Aeronautics, Astronautics and Aviation*, 2012, **44**, (3), pp 201-210.
7. NICOLAS, T., BREITSAMTER, C. and ADAMS, N.A. Numerical and experimental analysis of a generic fan-in-wing configuration, *J Aircraft*, 2009, **46**, (2), pp 656-666.
8. RICHASON, T.F., KATZ, J. and ASHBY, D.L. Unsteady panel method for flows with multiple bodies moving along various paths, *AIAA J*, 1994, **32**, (1), pp 62-68.
9. KATZ, J. and MASKEW, B. Unsteady low-speed aerodynamic model for complete aircraft configurations, *J Aircraft*, 1988, **25**, (4), pp 302-310.
10. DEGENNARO, A.M. Three-dimensional panel method hydrodynamic models of oscillating fins, *50th AIAA Aerospace Sciences Meeting including the New Horizons Forum and Aerospace Exposition*, AIAA 2012-0129, 2012, Nashville, Tennessee, US.
11. WIE, S.Y., LEE, S. and LEE, D.J. Potential panel and time-marching free-wake coupling analysis for helicopter rotor, *J Aircraft*, 2009, **46**, (3), pp 1030-1041.
12. LEISHMAN, J.G., BHAGWAT, J.M. and BAGAI, A. Free-vortex filament methods for the analysis of helicopter rotor wakes, *J Aircraft*, 2002, **39**, (5), pp 759-775.
13. HUBERSON, S., RIVOALEN, E. and VOUTSINAS, S. Vortex particle methods in aeroacoustics calculations, *J Computational Physics*, 2008, **227**, pp 9216-9240.
14. OPOKU, D.G., TRIANTOS, D.G., NITZSCHE, F. and VOUTSINAS, S.G. Rotorcraft aerodynamic and aeroacoustic modeling using vortex particle methods, *23rd International Congress of Aeronautical Sciences*, 2002, Toronto, Canada.
15. VOUTSINAS, S.G. Vortex methods in aeronautics: how to make things work. *Int J Computational Fluid Dynamics*, 2006, **20**, (1), pp 3-18.
16. WILLIS, D.J., JAIME, P. and JACOB, K.W. A combined PFFT-multipole tree code, unsteady panel method with vortex particle wakes, *Int J Numerical Methods in Fluids*, 2007, **53**, (8), pp 1399-1422.

https://doi.org/10.1017/aer.2017.109 Published online by Cambridge University Press

17. KATZ, J. and PLOTKIN, A. *Low-Speed Aerodynamics* (2nd ed), 2001, Cambridge University Press, Cambridge, England.
18. TAN, J.F. and WANG, H.W. Simulating unsteady aerodynamics of helicopter rotor with panel/viscous vortex particle method, *Aerospace Science and Technology*, 2013, **30**, (1), pp 255-268.
19. HE, C.J. and ZHAO, J.G. Modeling rotor wake dynamics with viscous vortex particle method, *AIAA J*, 2009, **47**, (4), pp 902-915.
20. COTTET, G.H. and KOUMOUTSAKOS, P. *Vortex Methods: Theory and Practice*, 2000, Cambridge University Press, Cambridge, England.
21. ELDREDGE, J.D., LEONARD, A. and COLONIUS, T. A general deterministic treatment of derivatives in particle methods, *J Computational Physics*, 2002, **180**, (2), pp 686-709.
22. HESS, J.L. Calculation of potential flow about arbitrary three dimensional lifting bodies, McDonnel Douglas MDC J5679-01, 1972, Long Beach, California, US.
23. CALABRETTA, J. A Three Dimensional Vortex Particle-panel Code for Modeling Propeller-airframe Interaction, MS thesis, California Polytechnic State University, California, US, 2010.
24. RICHASON, T.F., KATZ, J. and ASHBY, D.L. Unsteady panel method for flows with multiple bodies moving along various paths, *AIAA J*, 1994, **32**, (1), pp 62-68.
25. KINNAS, S.A. and HSIN, C.Y. Boundary element method for the analysis of the unsteady flow around extreme propeller geometries, *AIAA J*, 1992, **3**, (3), pp 688-696.
26. GAGGERO, S. VILLA, D. and BRIZZOLARA, S. RANS and panel method for unsteady flow propeller analysis, *9th International Conference on Hydrodynamics*, 2010, Shanghai, China, pp 564–569.
27. SMITH, B.E. and ROSS, J.C. Application of a panel method to wake-vortex/wing interaction and comparison with experimental data, NASA-TM-88337, 1987, Moffett Field, California, US.
28. ROBERT, J.M., WALKER, B.S. and MILARD, B.F. Experimental results for the eppler 387 airfoil at low Reynolds numbers in the Langley low-turbulence pressure tunnel, NASA TM4062, 1988, Hampton, Virginia, US.
29. RAHMAN, M.M., AGARWAL, R.K. and LAMPINEN, M.J. Wall-distance-free version of Spalart-Allmaras turbulence model, *AIAA J*, 2015, **53**, (10), pp 3016-3027.
30. MENTER, F.R. Two-equation eddy-viscosity turbulence models for engineering applications, *AIAA J*, 1994, **32**, (8), pp 1598-1605.
31. WALTERS, D.K. and LEYLEK, J.H. Computational fluid dynamics study of wake-induced transition on a compressor-like flat plate, *J Turbomachinery*, 2005, **127**, (1), pp 52-63.
32. CARADONNA, F.X. and TUNG, C. Experimental and analytical studies of a model helicopter rotor in hover, NASA TM-81232, 1981, Moffett Field, California, US.

https://doi.org/10.1017/aer.2017.109 Published online by Cambridge University Press